Characteristic-Based, Time-Dependent Maxwell Equation Solvers on a General Curvilinear Frame

J. S. Shang* and Datta Gaitonde†

U.S. Air Force Wright Laboratory, Wright-Patterson Air Force Base, Ohio 45433-7913

Four cell-centered, finite-volume characteristic-based procedures for solving time-dependent, three-dimensional Maxwell equations on a general curvilinear frame are developed and implemented. On a spherical coordinate system, these methods generate simulations of an oscillating electric dipole without wave reflection from the truncated computational domain. Through a comparative study, it is established that an upwind-biased third-order scheme demonstrates less dispersive and dissipative errors than second-order schemes.

Nomenclature

A	= coefficient matrix
B	= magnetic flux density
C	= coordinate transformation matrix
D	= electric displacement
E	= electric field strength
F_1, F_2, F_3	= vector components in flux-vector formulation
H	= magnetic field strength
i, j, k	= index of discretized volume
J	= electric current density
n	= index of temporal level of solution
R	= residual
r, θ, ϕ	= spherical coordinates
S	= similar matrix of diagonalization
t	= time
U	= dependent variables
V	= elementary cell volume
x, y, z	= Cartesian coordinates
α	= stage coefficient for Runge–Kutta integration
γ	= parameter in Runge–Kutta integration
ϵ	= electric permittivity
κ	= parameter in monotonic upwind-centered scheme for conservation laws (MUSCL) formulation
μ	= magnetic permeability
ξ, η, ζ	= coordinates of transformed space
ϕ_1	= parameter determining order of accuracy
Λ	= eigenvalue
∇	= gradient, backward difference operator
Δ	= discrete or forward difference operator

Subscripts

x, y, z	= components in or derivatives with respect to Cartesian coordinates

Superscripts

$+$	= vector associated with positive eigenvalue
$-$	= vector associated with negative eigenvalue
$\wedge$	= vector in curvilinear frame
$\sim$	= vector in locally orthogonal system
L	= variable on left side of interface
R	= variable on right side of interface

I. Introduction

UNSTEADY wave propagation and scattering phenomena in an electromagnetic field can be described completely by the time-domain Maxwell equations.[1,2] The system of partial differential equations is hyperbolic and constitutes an initial-value problem.[3] Since all associated eigenvalues are real, the initial values along characteristics propagate continuously throughout the infinite physical space. Unfortunately, numerical approximations to the time-dependent Maxwell equations with either the finite difference or the finite volume approaches must be carried out on a finite-sized domain, the outer surfaces of which become numerical boundaries. On such artificial boundaries, improperly specified numerical values may induce spurious wave reflections. The incurred numerical errors are known to lead to erroneous accumulation of radiating energy and unrealistic modulations of wave amplitude.[4,5] Since wave phenomena have a dominant direction of propagation, this fundamental dilemma of numerical simulation can be eliminated through eigenvalue and eigenvector analyses with characteristic formulation.[6-8]

The fundamental idea of the characteristic-based methods[9,10] for solving a hyperbolic equation system is derived from eigenvalue analysis of the governing equations. In numerical analysis, the well-posedness requirement and the stability of the discretized system are ultimately linked to the structure of the eigenvalues. Therefore, characteristic-based schemes often exhibit drastic improvements in numerical stability and accuracy over conventional numerical methods for wave motion simulations.[8-10] However, the characteristic-based formulation also has an inherent limitation in that the coefficient matrices of the governing equations, when written in flux vector form, can be diagonalized in only one dimension at a time.[10] The one-dimensional characteristics are exact when the principal axis of wave motion coincides with one of the coordinates. For computational electromagnetics, the orientation of wave motion is always known to be perpendicular to both the electric and magnetic field intensities, $E \times H$.[1,2] This unique feature can thus always be incorporated into the formulation by a general coordinate transformation.

In our previous efforts,[6-8] two characteristic-based, fractional-step, implicit and explicit finite difference methods have been successfully developed for solving three-dimensional, time-dependent Maxwell equations. Under controlled conditions, these numerical procedures have generated excellent solutions for a three-dimensional waveguide in comparison with the theoretical result.[1,2,8] If an electromagnetic wave motion can be manipulated to propagate along a coordinate, the one-dimensional characteristics are also the exact compatible conditions on the truncated boundaries, and the resulting simulation is the best achievable by numerical means. Reasonable simulations of an oscillating electric dipole have also been obtained.[8] The no-reflection condition is deduced from the one-dimensional characteristics. These invariant one-dimensional characteristics, when imposed as approximations at the outer surfaces of a three-dimensional computational domain, have demonstrated a degree of effectiveness beyond their range of validity.[6,8] Nevertheless,

this implementation can still introduce uncertain numerical error from the misalignment of wave motion and coordinate orientation. The error can be removed by an appropriate coordinate rotation to align with the principal axis of wave motion. Equally important in practical applications of computational electromagnetics (CEM) is flexibility in accommodating complex geometry. This requires formulation on a general curvilinear coordinate system.

The present effort develops a versatile numerical tool for CEM by casting the three-dimensional, time-dependent Maxwell equations in a general curvilinear frame of reference. The system of equations is first written on the Cartesian frame; then a coordinate transformation is introduced to accept a wide range of arbitrary geometric shapes. On the wave scattering surface, a locally orthogonal body conformal coordinate system can greatly facilitate boundary condition implementation.[1,2] To eliminate spurious wave reflection, the coordinates can also be rotated to align with the principal axis of wave motion at the outer region of the computational domain. In this manner, the characteristic data can always be effectively utilized to establish the exact no-reflection condition.

Numerical simulations of the Maxwell equations can be generated either by finite difference or finite volume schemes.[5,8] For conservative laws like the Navier–Stokes equations, the basic difference between these two procedures depends upon whether the equation is solved in integral or differential form.[11] The Maxwell equations include a conservation law only for electric charge and current densities.[1,2] This constitutive relation is not independent from the other basic law and usually is not required to be solved. Hence, for CEM applications, there is no conceptual difference between these approaches, and the choice is based upon convenience. However, for the hyperbolic differential systems, piecewise continuous and nonanalytic solutions are admissible.[3] Finite volume procedures in computational fluid dynamics (CFD) applications have demonstrated a superior quality in treating discontinuous fields[11–14] and may be preferred for CEM.

With a coordinate transformation, the uncoupling suggested in Ref. 8 introduces a nonhomogenous term. This added complexity to the characteristic formulation of the Maxwell equations no longer permits the system of one-dimensional equations to be written as a true Riemann problem.[6,8] There is therefore no advantage in solving the uncoupled scalar equations. Nevertheless, because of the potential for numerical efficiency by uncoupling, the required eigenvector analysis and rederivation of the Maxwell equations for the finite difference procedure will continue to be pursued in future.

The present effort adopts the cell-centered, finite volume MUSCL (monotonic upwind-centered scheme for conservation laws) approach of van Leer[15] extending a basic procedure to higher order accuracy. The gist of the algorithm is based on the reconstruction of the solution from piecewise continuous data and subsequent upwinding approximation according to the eigenvalue structure at the cell faces. A wide range of numerical algorithms both in temporal and spatial integration are investigated. Numerical simulations are validated by comparison with theoretical results.[1,2]

II.   Analysis

Governing Equations

The time-dependent Maxwell equations for the electromagnetic field in free space can be written as[1,2]

$$\frac{\partial(\mu H)}{\partial t} + \nabla \times E = 0 \tag{1}$$

$$\frac{\partial(\epsilon E)}{\partial t} + \nabla \times H = -J \tag{2}$$

$$\nabla \cdot B = 0, \qquad B = \mu H \tag{3}$$

$$\nabla \cdot D = 0, \qquad D = \epsilon E \tag{4}$$

The only conservative law for electric charge and current densities is

$$\frac{\partial \rho}{\partial t} + \nabla \cdot J = 0 \tag{5}$$

Although the above equation is regarded as a fundamental law of electromagnetics, it is derivable from the generalized Ampere circuit
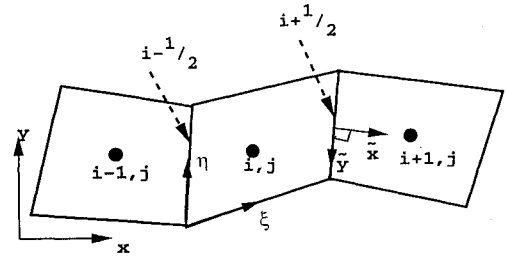

Fig. 1   Schematic of curvilinear coordinate system.

law and the Gauss laws for electric fields.[1,2] Equations (1) and (2) are independent and constitute the basic equations of computational electromagnetics.

The system of governing equations cast in vector form on a Cartesian frame is

$$\frac{\partial U}{\partial t} + \frac{\partial F_1}{\partial x} + \frac{\partial F_2}{\partial y} + \frac{\partial F_3}{\partial z} = -J \tag{6}$$

where

$$U = \begin{Bmatrix} B_x \\ B_y \\ B_z \\ D_x \\ D_y \\ D_z \end{Bmatrix}, \qquad F_1 = \begin{Bmatrix} 0 \\ -D_z/\epsilon \\ D_y/\epsilon \\ 0 \\ B_z/\mu \\ -B_y/\mu \end{Bmatrix} \tag{7}$$

$$F_2 = \begin{Bmatrix} D_z/\epsilon \\ 0 \\ -D_x/\epsilon \\ -B_z/\mu \\ 0 \\ B_x/\mu \end{Bmatrix}, \quad F_3 = \begin{Bmatrix} -D_y/\epsilon \\ D_x/\epsilon \\ 0 \\ +B_y/\mu \\ -B_x/\mu \\ 0 \end{Bmatrix}, \quad J = \begin{Bmatrix} 0 \\ 0 \\ 0 \\ J_x \\ J_y \\ J_z \end{Bmatrix} \tag{8}$$

To accommodate a wide range of scattering shapes, a general curvilinear coordinate transformation (Fig. 1) is needed to define a one-to-one relationship between two sets of temporal and spatially independent variables. For now, the coordinate system transformation is limited to the spatially independent variables only:

$$\xi = \xi(x, y, z)$$
$$\eta = \eta(x, y, z) \tag{9}$$
$$\zeta = \zeta(x, y, z)$$

Equation (6) may be transformed to the following form in the (ξ, η, ζ) space:

$$\frac{\partial \hat{U}}{\partial t} + \frac{\partial \hat{F}_1}{\partial \xi} + \frac{\partial \hat{F}_2}{\partial \eta} + \frac{\partial \hat{F}_3}{\partial \zeta} = -\hat{J} \tag{10}$$

The transformed dependent variables and the flux vectors of Eq. (10) are given in the following:

$$\hat{U} = UV, \qquad \hat{J} = JV$$
$$\hat{F}_1 = (\xi_x F_1 + \xi_y F_2 + \xi_z F_3)V$$
$$\hat{F}_2 = (\eta_x F_1 + \eta_y F_2 + \eta_z F_3)V \tag{11}$$
$$\hat{F}_3 = (\zeta_x F_1 + \zeta_y F_2 + \zeta_z F_3)V$$

where V denotes the discretized cell volume and is identical to the inverse Jacobian of the coordinate transformation.

The preceding system of equations is solved by discretizing the physical space into contiguous cells and balancing the flux vectors on the faces of the cell. Thus in discretized form, the integration procedure degenerates into evaluation of the sum of all fluxes aligned with surface area vectors. In the present work, a cell-centered, finite volume, unstaggered, collocated approach is implemented. Thus

all field vectors are located at the centers of the cell volumes. For a first-order approximation, these values represent the solution in the entire cell. The splitting approach is first described with reference to Eq. (6) on a Cartesian system. This is followed by the extension to the curvilinear coordinate system of Fig. 1 and Eq. (10).

In discretized form, Eq. (6) is replaced by a difference formulation astride the cell surface:

$$\frac{\Delta U}{\Delta t} + \frac{\Delta F_1}{\Delta x} + \frac{\Delta F_2}{\Delta y} + \frac{\Delta F_3}{\Delta z} - J = \frac{\Delta U}{\Delta t} + R = 0 \qquad (12)$$

where the continuous operators $\partial/\partial t$, $\partial/\partial x$, $\partial/\partial y$, $\partial/\partial z$ have been replaced by the discrete operators $\Delta/\Delta t$, $\Delta/\Delta x$, $\Delta/\Delta y$, $\Delta/\Delta z$ and R denotes the residual of the discretized approximation.

The spatial discretization terms may be described by considering a typical term of Eq. (12), $\Delta F_1/\Delta x$. In the finite volume approach, the flux vector balance is approximated as

$$\frac{\Delta F_1}{\Delta x} = \frac{F_{1,i+(1/2)} - F_{1,i-(1/2)}}{\Delta x} \qquad (13)$$

The construction of the fluxes $F_{1,i\pm(1/2)}$ at the interfaces $i \pm \frac{1}{2}$ from the known values of the solution vector at the adjacent cells determines the salient features, particularly the accuracy of a particular algorithm. In the present effort, the equivalent of the Steger–Warming method[9] is employed in which the flux at an interface is written as a superposition of two components, F_1^+ and F_1^-, which are uniquely associated with the signs of the eigenvalues of the flux Jacobian matrix $\partial F_1/\partial U$. Physically, this procedure reflects the direction of signal propagation, or the right or left running wave in the domain of influence.[3,6,9] Focusing on the cell surface, $i + \frac{1}{2}$, a first-order approximation is obtained as

$$F_{1,i+1/2} = F_1^+(U_i) + F_1^-(U_{i+1}) \qquad (14)$$

Note that F_1^+ and F_1^- are evaluated at U_i and U_{i+1}, respectively, according to a windward scheme. A simple algebraic calculation shows that the fluxes F_1, F_2, and F_3 are homogeneous of order 1.[16] Thus, $F_1 = AU$, where the flux Jacobian A is given by

$$A = \frac{\partial F_1}{\partial U} = \begin{bmatrix} 0 & 0 & 0 & 0 & 0 & 0 \\ 0 & 0 & 0 & 0 & 0 & -\frac{1}{\epsilon} \\ 0 & 0 & 0 & 0 & \frac{1}{\epsilon} & 0 \\ 0 & 0 & 0 & 0 & 0 & 0 \\ 0 & 0 & \frac{1}{\mu} & 0 & 0 & 0 \\ 0 & -\frac{1}{\mu} & 0 & 0 & 0 & 0 \end{bmatrix} \qquad (15)$$

Since the Maxwell equations constitute a hyperbolic system, all eigenvalues of the coefficient matrix A are real although containing multiplicities, $\Lambda = \text{diag}\{-1/\sqrt{\epsilon\mu}, -1/\sqrt{\epsilon\mu}, 1/\sqrt{\epsilon\mu}, 1/\sqrt{\epsilon\mu}, 0, 0\}$. Nevertheless, linearly independent eigenvectors can still be found. The detailed structure of the similarity matrices of diagonalization S and S^{-1} may be found in the literature.[6-8] The positive and the negative components of a flux correspond to the positive and the negative eigenvalues, respectively:

$$F_{1,i+(1/2)}^+(U_i) = S(U_i)\Lambda^+(U_i)S^{-1}(U_i) \qquad (16)$$

$$F_{1,i+(1/2)}^-(U_{i+1}) = S(U_{i+1})\Lambda^+(U_{i+1})S^{-1}(U_{i+1}) \qquad (17)$$

where $\Lambda^+ = \text{diag}\{0, 0, 1/\sqrt{\epsilon\mu}, 1/\sqrt{\epsilon\mu}, 0, 0\}$ and $\Lambda^- = \text{diag}\{-1/\sqrt{\epsilon\mu}, -1/\sqrt{\epsilon\mu}, 0, 0, 0\}$.

The splitting of the transformed fluxes in Eq. (10) is greatly facilitated by the introduction of a third orthogonal local system for each face of the mesh.[12] In this new system, the necessary eigenvalue and eigenvector analyses required for flux splitting as well as the reverse mapping into the curvilinear coordinates are well known.[6] The procedure of Ref. 12 is illustrated by examining the construction of $\hat{F}_1^\pm$ required on face $i + \frac{1}{2}$. A local system normal to this face ($\tilde{x}\tilde{y}\tilde{z}$) is

defined with $\tilde{x}$ in the direction of the surface normal, $\nabla\xi$. The terms $\tilde{y}$ and $\tilde{z}$ are nonuniquely defined to lie orthogonal to each other in the $i + \frac{1}{2}$ plane (see Fig. 1 for a two-dimensional case). Let C denote the transformation matrices mapping the six-component vector U in the original Cartesian reference frame (x, y, z) into $\tilde{U}$ in the new local system $\tilde{x}, \tilde{y}, \tilde{z}$. Thus, the components of C are the direction cosines or components of the unit vectors of the new system, and because of the orthogonal nature of the two coordinates, the inverse transformation C^{-1} is simply the transpose of C.[3] The basis of the splitting method lies in the fact that the term $\tilde{F}_1 = C\hat{F}_1$, expressing the components of $\hat{F}_1$ in the $\tilde{x}\tilde{y}\tilde{z}$ system, has the same functional form as the original vector F_1, except for a constant $\nabla\xi V$ representing the area of the $i + \frac{1}{2}$ face. Thus, for example, $\tilde{F}_1$ may be constructed by simply replacing D_z in Eq. (7) by $\tilde{D}_z$. This structural similarity provides an elegant means of splitting the vector without the tedious effort for diagonalization in the general curvilinear coordinates.[12] This advantage of finite volume formulation over that of the finite difference is significant for the present endeavor. Since the functional forms of $\tilde{F}_1$ and F_1 are identical, the eigenvalues of $\tilde{F}_1$ may be easily written following Ref. 8 and $\hat{F}_1$ may be split as

$$\hat{F}_1^\pm = C^{-1}C\hat{F}_1^\pm = C^{-1}\tilde{F}_1^\pm \qquad (18)$$

Therefore at any interface

$$\hat{F}_1 = C^{-1}\tilde{S}^{-1}\Lambda\tilde{S}\tilde{U} = C^{-1}\tilde{S}^{-1}[\Lambda^- + \Lambda^+]\tilde{S}\tilde{U} = \hat{F}_1^+ + \hat{F}_1^- \qquad (19)$$

The similar matrices of diagonalization $\tilde{S}$ have similar form to those in Cartesian coordinates and can be found in earlier works.[6-8] The calculation details of flux splitting is outlined later. The fluxes $\hat{F}_2$ and $\hat{F}_3$ required for the $j + \frac{1}{2}$ and $k + \frac{1}{2}$ faces, respectively, may be obtained in a similar fashion. The splitting is thus carried out normal to each face in the transformed system, and the resulting three-dimensional flux is balanced by superposition of one-dimensional splitting operators.

Spatial Integration Procedures

The characteristic-based formulation has an inherent limitation in that the diagonalization of coefficient matrices is restricted to one dimension in time and space.[8-10] As already described, the extension to two- and three-dimensional space is achieved by considering one dimension at a time. The formal order of accuracy of the split-flux method in each direction may be ascertained by considering a one-dimensional equation, specifically the model wave equation

$$u_t + f_x = u_t + (cu)_x = 0, \qquad c = \text{const} > 0 \qquad (20)$$

Then,

$$f_{i+(1/2)}^+ = cu_i, \qquad f_{i+(1/2)}^- = 0$$

$$f_{i-(1/2)}^+ = cu_{i-1}, \qquad f_{i-(1/2)}^- = 0$$

and

$$\frac{\Delta cu}{\Delta x} = \frac{(cu)_i - (cu)_{i-1}}{\Delta x} \qquad (21)$$

which is clearly a one-sided backward windward formula with a formal leading term truncation of $\mathcal{O}(\Delta x)$.

The extension to higher order accuracy is achieved in this work with the MUSCL approach of van Leer.[15] The essence of this method is to reconstruct the solution from the piecewise data of each cell volume at the intermediate adjacent locations of the cell interface with a higher degree polynomial provided by Taylor series expansions. Considering again a scalar variable as a function of x, the value in cell i may be written as

$$u(x) = u_i + \frac{\partial u}{\partial x}\bigg|_i (x - x_i) \qquad (22)$$

The slope $\partial u/\partial x$ is obtained with data at the cell centers $i - 1$, $i, i + 1$—greater stencils are not considered at the present time—to obtain an approximation to the slope of u at the cell center:
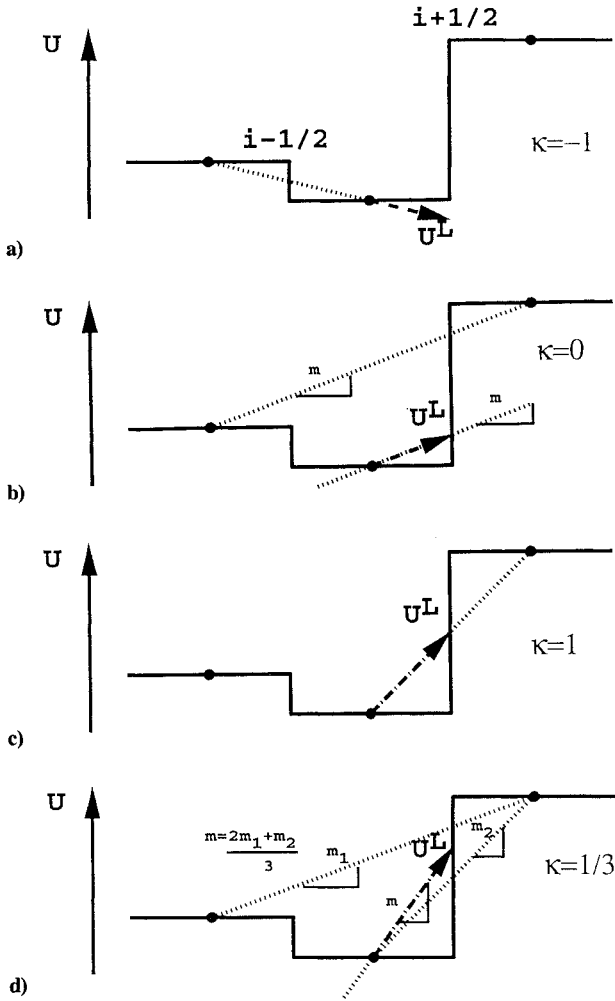
$$u_x|_i = s(u_{i-1}, u_i, u_{i+1}) \qquad (23)$$

Fig. 2   Evaluation of L state at $i + \frac{1}{2}$ with various κ values.

Fig. 3   Comparison of trace of electric field (first-order solution).

method degenerates into the first-order accurate approximation. For $\phi_1 = 1$, the relevant terms in the modified equation are[17]

$$c\frac{\Delta u}{\Delta x} = c\frac{\partial u}{\partial x} + \frac{\Delta x^2}{12}c\,(3\kappa - 1)\,\frac{\partial^3 u}{\partial x^3} + \frac{\Delta x^3}{8}c\,(1 - \kappa)\,\frac{\partial^4 u}{\partial x^4} \quad (28)$$

Four distinct second- and higher order accurate numerical schemes can be derived by assigning different values to κ. The relevant slope evaluations to obtain $U^L_{(i+1/2)}$ are noted in Fig. 2. Here, $\kappa = -1$ leads to a two-point windward scheme that uses the data in i and $i - 1$ cells to derive the interface value $u^L_{i+1/2}$. For this procedure, the leading truncation error term is an odd-order derivative. Thus the dispersive error may be expected to dominate, although the dissipative error is also the greatest among the four possibilities. For $\kappa = 0$, the slope approximation demonstrated in Fig. 3 recovers the Fromm scheme.[18] If $\kappa = 1$, the spatially central scheme is recovered. Since the fourth-order dissipative term is suppressed, the central scheme is susceptible to parasitic odd-even point decoupling.[17] A third-order upwind-biased scheme emerges with $\kappa = \frac{1}{3}$. This scheme has an even-order leading truncation error term; the numerical dispersion shall be less pronounced.

where s is a function defined by the truncated Taylor series expansion according to the cell center values used. For example, a central approximation to s reads

$$s(u_{i-1}, u_i, u_{i+1}) = \frac{u_{i+1} - u_{i-1}}{2\,\Delta x} \quad (24)$$

Once the variation specified by Eq. (22) is chosen, the values of the dependent variable may be reconstructed on either side of each interface. Let u^L and u^R denote these values on either side of the interface $i + \frac{1}{2}$. Note that the value of u^R can be constructed by the slope at $i + 1$ using the stencil $i, i + 1$, and $i + 2$. These reconstructed solutions at the cell surface are then used to compute the positive and the negative fluxes across the cell interface. For the flux vector F_1,

$$F_{1,i+(1/2)} = F_1^+(U^L) + F_1^-(U^R) \quad (25)$$

A wide range of variation of the function s in Eq. (26) may be described by the κ schemes,[17] in which the L and R states are acquired by the formulas

$$U^L_{i+(1/2)} = U_i + \tfrac{1}{4}\phi_1[(1 - \kappa)\nabla + (1 + \kappa)\Delta]U_i \quad (26)$$

$$U^R_{i+(1/2)} = U_{i+1} - \tfrac{1}{4}\phi_1[(1 + \kappa)\nabla + (1 - \kappa)\Delta]U_{i+1} \quad (27)$$

where $\nabla U_i = U_i - U_{i-1}$ and $\Delta U_i = U_{i+1} - U_i$. The parameters ϕ_1 and κ control the order of accuracy of the derivative evaluation. The flux at any interface $i + \frac{1}{2}$ is easily computed from Eqs. (25–27).

For the simple wave model equation (20), the truncated series expansion of the spatial derivative $c\,\partial u/\partial x$ can provide additional information of aliasing or quasi-physical errors as well as the formal order of accuracy for the chosen MUSCL scheme. If $\phi_1 = 0$, the
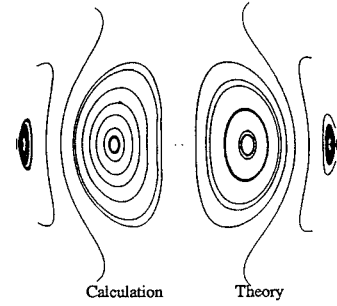
Time Integration Procedures

In the previous discussion, several spatial integration procedures were developed ranging from first-order windward to third-order upwind biased. To achieve consistent numerical accuracy both in time and space, compatible higher temporal integration processes are outlined. In general, second- or higher order temporal resolution is achievable through multiple time-step or time-level schemes[9–11] or equivalent fractional-step methods[8,19] for finite-volume approaches. One-step schemes are attractive not only because of lower memory requirements but also because no special start-up procedures are necessary. In the present effort, a Runge–Kutta family of single-step, multistage procedures[20] is employed permitting variable order of time accuracy in one programming procedure. Further, though only the first-order derivative evaluations are involved, results are equivalent in accuracy to the higher order Taylor formulas.[20]

The implementation for CEM calculations is similar to that for CFD. The present development follows that of Ref. 21. The set of partial differential equations represented by Eq. (12) is interpreted as a system of ordinary differential equations in time. All of the spatial derivatives as well as the source term are lumped into the residual R, which may be computed in each cell with one of the schemes previously outlined. This viewpoint permits a separate examination of the spatial and temporal integration algorithms on issues of conservation, spatial resolution, and consistency. A single-step multistage scheme may be defined as

$$\begin{aligned} U^0 &= U^n \\ U^1 &= U^0 - \alpha_1\,\Delta t\,R^0 \\ &\;\;\vdots \\ U^{m-1} &= U^0 - \alpha_{m-1}\,\Delta t\,R^{m-2} \\ U^m &= U^0 - \alpha_m\,\Delta t\,R^{m-1} \\ U^{n+1} &= U^m \end{aligned} \quad (29)$$

This represents an m-stage scheme giving the solution at time level $n + 1$ from the known solution at time level n. The values of R are

obtained from a linear combination of residuals at earlier stages. In general, at stage s,

$$R^s = \sum_{i=0}^{i=s-1} \gamma_{si} R(U^i), \qquad \sum_{i=0}^{i=s-1} \gamma_{si} = 1 \qquad (30)$$

A number of schemes may be obtained from the preceding formulation. For example, the single-stage scheme ($m = 1$) with $\alpha_1 = 1$ gives the standard first-order accurate forward Euler formula. In the present work, the two-stage, formally second-order accurate method is used:

$$U^0 = U^n$$

$$U^1 = U^0 - \alpha_1 \Delta t R(U^0), \qquad \alpha_1 = 1$$

$$U^2 = U^0 - \alpha_2 \Delta t [R(U^0) + R(U^1)], \qquad \alpha_2 = 0.5$$

$$U^{n+1} = U^2$$

For schemes with more stages, considerable simplicity may be achieved without additional memory requirements by choosing $\gamma_{si} = \delta_{(s-1)i}$, where δ is the Kronecker delta function. This permits code operation at higher Courant–Friedrichs–Lewy (CFL) numbers. A scheme commonly employed in CFD is the five-stage scheme with $\alpha_1, \ldots, \alpha_5$ taking values $\frac{1}{4}, \frac{1}{6}, \frac{3}{8}, \frac{1}{2}, 1$.

III. Numerical Procedure

The three-dimensional, finite volume numerical procedures are validated by direct comparison with theoretical results of an oscillating electric dipole for which the closed-form solution is known.[1,2] From these specific comparisons, the salient features for different orders of approximation are assessed on varying cell volume dimensions. The comparison of time-dependent solutions is performed on both the spatial variation at fixed time and the temporal variation at a fixed point in space.

For the oscillating electric dipole simulation, the pulsing phenomenon was induced by a sinusoidal point source current vector. The pulsating source is described by an amplitude of unity and a wavelength equal to the half-radius of the spherical computational domain, $r/2$. Since the Maxwell equations constitute a hyperbolic system, the only physically meaningful initial condition required is the total induced field at the dipole. However, in order to alleviate the extremely small time-step restriction dictated by the finest cell volume near the coordinate origin, the initial conditions were imposed for a few cells immediately adjacent to the dipole. All simulations were initiated by the oscillating dipole in the middle of the quiescent computational space. Therefore at the beginning, the electromagnetic waves appear in the computational domain as a pulse. The entire induced field will then continuously evolve with the pulsating source. In all computations, periodic wave motion was established after a fraction of one characteristic time, T_{ch}, which is defined as the time elapse for a pulsing wave to traverse the entire computational domain.

The far-field boundary condition on the truncated domain is described simply by the zero incoming flux component:

$$\hat{F}_1^-(r_b, \theta, \phi) = 0 \qquad (31)$$

where r_b denotes the radius of the outer boundary. For the dipole formulation on the spherical coordinate, this boundary value is also the exact one-dimensional compatibility condition. Since the numerical boundaries of circumferential and the azimuthal directions merely reflect a continuous field, arrays of two overlapping cells are sufficient to enforce the functional continuity requirement.

During the initial phase of the present effort, preliminary computations were performed on an Iris 4D/440 VG. A $24 \times 24 \times 48$ spherical mesh system was used. The radial distance was scaled by a unit length, $0.0 < r < 1.0$; the angular displacements in circumferential and azimuthal directions were given by an interval of 9.00 deg and 8.57 deg, respectively. The first-order flux reconstruction combined with the Euler forward single-time-step algorithm

yielded a data processing rate of 3.20×10^{-4} s per cell per time step. For three-dimensional simulations, the maximum allowable time step was limited by the theoretical CFL number of $\sqrt{\frac{1}{3}}$, and the computation was sustainable for a substantial period.

The major portion of present results for numerical validation were generated on a Cray XMP216 system. The numerical accuracy assessment was performed on three mesh systems: Coarse, medium, and fine cell dimensions were defined by the systems of $9 \times 13 \times 18$, $19 \times 23 \times 34$, and $39 \times 43 \times 64$ cells. Excluding the overlapping arrays on the numerical boundaries, these systems reflect successive volumetric refinement by a factor of 8. The medium-size cell structure has similar angular increments to that of the preliminary calculation; however the range of radial distance was reduced by a factor of 2, $0.1 < r < 0.5$. Thus, calculations on the coarsest mesh ($9 \times 13 \times 18$) were still supported by a comparable cell volume to the preliminary results. The data processing rate on the XMP216 is 1.93×10^{-5} s per cell for the two-stage scheme. This is about 32 times lower than that of the Iris 4D/440 VG on a per-mesh point-stage basis.

IV. Discussion of Results

Figure 3 presents the electric field with the first-order accurate procedure on the $24 \times 24 \times 48$-mesh system at an instance $t = 2T_{ch}$. The numerical and theoretical results are projected side by side on a plane of symmetry. Within the known truncation error constraint, the numerical traces of the electric field are identical to the classical results.[1,2] The present result shows significant improvement over the earlier results obtained on a Cartesian frame.[8] The observed deviation in secondary structure of the electric field between theory and calculation is completely absent.[8] This finding serves as a direct substantiation to the assertion that when the transformed coordinate is aligned with the direction of wave movement, the one-dimensional compatibility relation is redeemed and the exact no-reflection condition is obtainable on a truncated computational boundary.

The comparative study of the entire magnetic field by simulation and theory is depicted in Fig. 4. This instantaneous time exposure is taken when the second pulse is exiting the computational space. Traces of the two magnetic fields are projected on the equatorial plane of the spherical coordinate. All magnetic lines appear as a series of concentric circles perpendicular to the direction of the alternating point current source. No detectable discrepancy from each other is noted, even in the location adjacent to the singular dipole where the numerical simulation receives the initial values. In short, the numerical simulation demonstrates that no wave reflection is incurred at the truncated boundary.

A specific comparison of the numerical magnetic field intensity with theory is depicted in Fig. 5. The field intensity distribution along a radial coordinate is recorded at the same instant as that in Figs. 3 and 4. The singular behavior of the magnetic field is clearly exhibited. Both the x and the y components reveal correctly the anticipated inverse-square power decay along the radial direction. The theory indicates a zero magnetic z component, whereas the numerical result reveals an error of the order of magnitude of 10^{-4}. Overall, excellent agreement is observed between the theoretical and the simulated results.

The corresponding comparison of electric fields is given in Fig. 6. Noticeable numerical errors begin to appear in comparison with
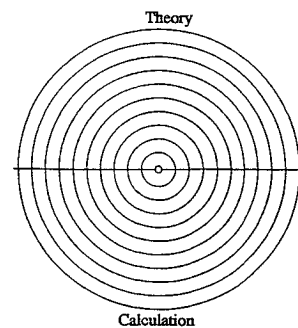

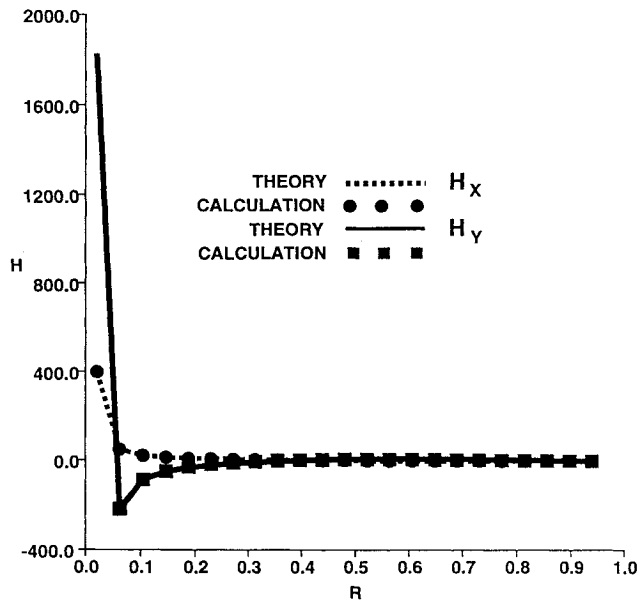Fig. 4 Comparison of trace of magnetic field (first-order solution).

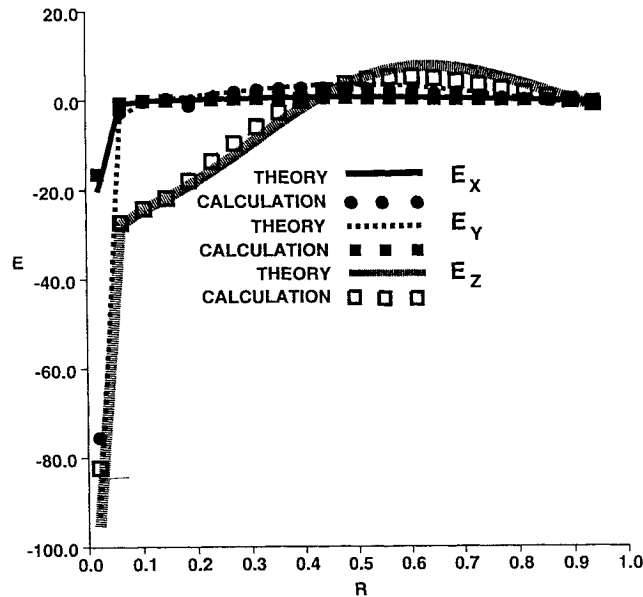**Fig. 5 Comparison of magnetic field in space, $T = 2.0$ (first-order solution).**

Fig. 6 Comparison of electric field in space, $T = 2.0$ (first-order solution).

Fig. 7 E_r, E_θ, and H_ϕ profiles at $r = 0.246$, $\theta = 69.5$ deg, $\phi = 167$ deg on coarse mesh.

the closed form result. The asymptotic solution contains a leading inverse cubic power term at the dipole that is extremely demanding in numerical duplication on a rather coarse cell dimension. The simulated z component of the electric field shows the most significant deviation from the theoretical result. The maximum numerical error is about 4.2%.

The preceding illustrations, particularly those examining the spatial variation at a given instance, demonstrate that the lower order accurate approach is incapable of meeting the demanding accuracy requirement for CEM. The subsequent discussion is focused on the higher order schemes developed earlier. In this regard, since the temporal response of a given numerical method to the highly oscillating wave motions is critical, an alternative approach is to conduct the comparative study by scanning the time variation at a fixed point in space.

The temporal behavior of radial and circumferential components of the electric field and the azimuthal component of the magnetic field at a point are monitored for all algorithms considered. Numerical simulations were sustained for the period of two characteristic times. A two-stage Runge–Kutta integration for temporal
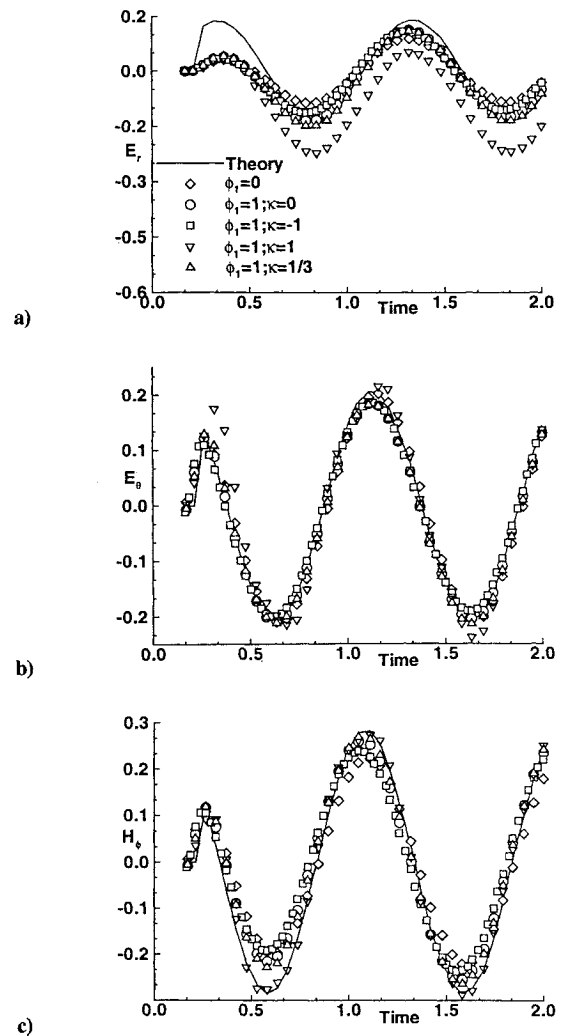
advancement is uniformly applied at a CFL number of unity to yield a second-order accurate solution in time.[20] Since the initial condition for the entire domain was undisturbed and the pulsating wave speed is finite, the calculations require a transient period to adjust to the impulse start. The transient period is estimated to persist over a third wave length of the oscillating phenomenon.

In Fig. 7, five numerical solutions generated on the coarse mesh system ($9 \times 13 \times 18$), and the theoretical results are presented together. It is clearly indicated that the first-order results bear the most dissipative and dispersive errors. The consistent phase lag is also easily detectable. The rather erratic solutions by the spatially central scheme ($\kappa = 1$) can be anticipated in which the physically meaningful information of wave propagation is ignored by this algorithm. It is remarkable that the basically unstable scheme was able to sustain for the entire period of simulation. A small but perceptible leading phase error was also observed for the rest of the higher order procedures. Unfortunately, quantification of these dispersive errors is uncertain for three-dimensional calculations. The upwinded second-order accurate schemes, including the two-point windward ($\kappa = -1$) and the Fromm methods ($\kappa = 0$) as well as the third-order upwind-biased method ($\kappa = 1/3$) exhibit progressively improved agreement with the theory. The maximum deviation of the third-order results from the theory appears in the prediction of the azimuthal magnetic component (7.4%).

Numerical solutions of the electromagnetic field obtained from the medium-size cell volume ($19 \times 23 \times 34$) are depicted in Fig. 8. The number of cells in use is deemed to be the minimum in adequately resolving the periodic motion; each wavelength is being resolved by 10 cells.[4,5] In the absence of dissipative additions, the parasitic odd-even point decoupling behavior of the spatially central
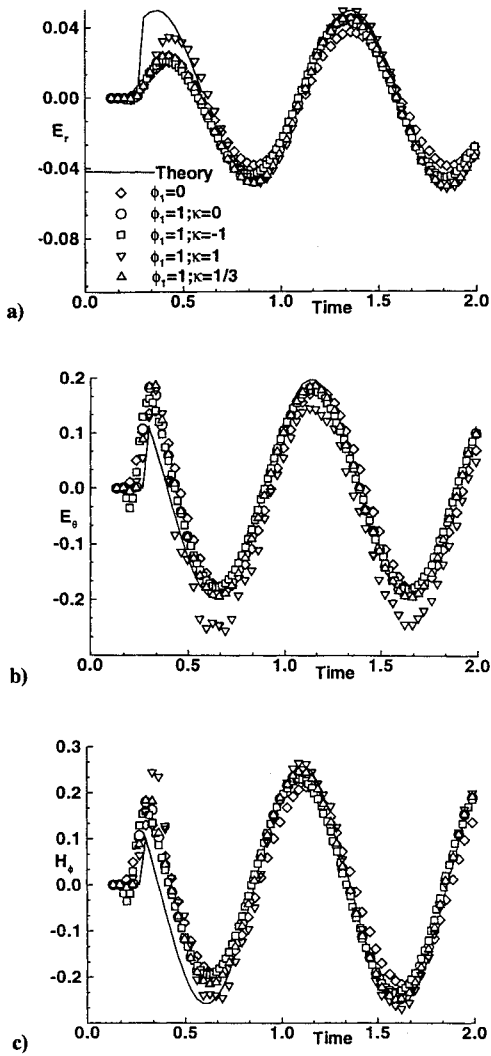
Fig. 8 E_r, E_θ, and H_ϕ profiles at $r = 0.277$, $\theta = 80.5$ deg, $\phi = 174$ deg on medium mesh.

For the electric field, the leading term singularity is proportional to the inverse cubic power of the radial distance from the pulse center. The asymptotic behavior of the magnetic intensity is less drastic than that of the electric field, but the singularity is still described by the inverse square power of r.[1,2] The numerical resolution requirement in reproducing this rapidly varying physical phenomenon is extremely demanding. The detailed analysis for dispersive and dissipative errors of three-dimensional unsteady computations is uncertain and requires continuing effort.

As a specific illustration that the characteristic-based methods are capable of eliminating wave reflection from the truncated numerical boundary, the electromagnetic field is depicted in Fig. 10. This set of calculations was obtained on the medium-mesh system at time, $T = 2.0$. The radial and the circumferential components of electric intensity as well as the azimuthal component of magnetic intensity in the outer edge of the computational space are presented together with the theory. All results generated by the first-order windward, the second-order Fromm, and the third-order upwind-biased schemes are given along a ray defined by $\theta = 37$ deg and $\phi = 30$ deg for the range of radius of $0.2 < r < 0.5$. The numerical solutions of the magnetic field show a uniformly closer affinity to the theoretical result as a reflection of the lower degree of singularity of the asymptotic expression. Although these numerical results reflect different orders of approximations, they unquestionably demonstrate that no wave is reflected from the truncated numerical boundary. In short, the present effort has convincingly shown that the no-reflection wave condition on a truncated numerical domain can be achieved by the characterisitic-based algorithm on a judiciously constructed coordinate system.
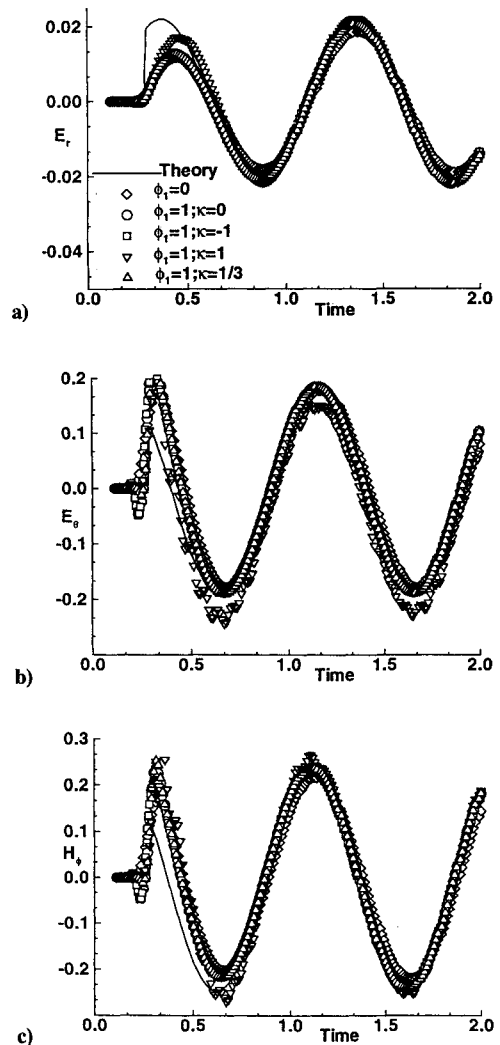

scheme again stands out. Therefore, its numerical accuracy will no longer be assessed with the others. As expected, numerical accuracy of the four methods can be rated in the following ascending order: the first order, the second-order windward, the Fromm, and the third-order upwind-biased scheme. The maximum deviation of the upwind-biased method for predicting radial and circumferential components of the electric field is 0.20 and 1.0%, respectively. The azimuthal component of the magnetic intensity is underpredicted by 3.49%, in comparison with the theory.

The final comparison of all numerical schemes on the finest cell volume is given by Fig. 9. All higher order solutions have reached excellent agreement with the theoretical results. The third-order upwind-biased scheme predicts the radial and the circumferential components of the electric intensity within the absolute values of 0.0001 and 0.004 at their local minima. The maximum discrepancy between theory and calculation for the azimuthal component of magnetic intensity is limited to the value of 0.005. The two second-order schemes also yield solutions of comparable accuracy with only slightly greater deviations from the theory. Based on the present study, the Fromm scheme has produced a superior result than the second-order windward method. Understandably, the first-order windward method yielded the least accurate results, as has been noted previously. For reason of completeness, the spatially central procedure is included here. The parasitic even-odd decoupling pattern of solutions becomes even more pronounced; numerical results by this method probably are not physically meaningful.

Finally, the accuracy assessment of present numerical results can be viewed in light of the inherent singular behavior of the dipole.

Fig. 9 E_r, E_θ, and H_ϕ profiles at $r = 0.289$, $\theta = 85.4$ deg, $\phi = 177$ deg on fine mesh.
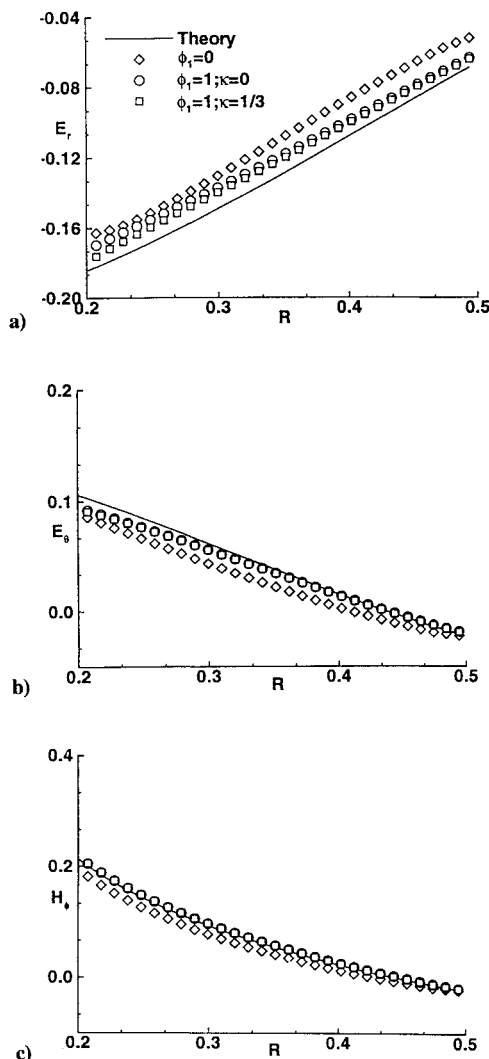
Fig. 10 E_r, E_θ, and H_ϕ profiles at $T = 2.0, \theta = 37$ deg, $\phi = 30$ deg on medium mesh.

V. Conclusions

A series of cell-centered, finite volume schemes based on the MUSCL approach have been systematically and successfully developed to solve the time-dependent Maxwell equations on a general curvilinear frame. All higher order methods and particularly the third-order method demonstrate the potential for further development.

On the spherical coordinate system, the direction of wave propagation induced by a three-dimensional oscillating dipole is aligned with the radial coordinate. Under this condition, the characteristic-based scheme is able to provide an exact no-reflection wave

condition on the truncated computational domain. The present numerical simulations substantiate this observation.

References

[1]Harrington, R. R., *Time-Harmonic Electromagnetic Fields*, McGraw–Hill, New York, 1961.

[2]Jordan, E. C., *Electromagnetic Waves and Radiating System*, Prentice–Hall, Englewood Cliffs, NJ, 1960.

[3]Courant, R., and Hilbert, D., *Methods of Mathematical Physics, Vol. II: Partial Differential Equations*, Interscience, New York, 1965.

[4]Anderson, D. A., "Interdisciplinary Applications of Simulation Computational Fluid Dynamics (CFD) and Radar Cross-Section (RCS)," AFATL-TR-88-1987, AF Armament Directorate, Eglin AFB, June 1989.

[5]Shankar, V., Hall, W. F., and Mohammadian, A. H., "A Time-Domain Differential Solver for Electromagnetic Scattering Problems," *Proceedings of Institute of Electrical and Electronics Engineers*, Vol. 77, No. 5, 1989, p. 709.

[6]Shang, J. S., "Characteristic-Based Methods for the Time-Domain Maxwell Equations," AIAA Paper 91-0606, Jan. 1991.

[7]Shang, J. S., "Characteristic-Based Algorithm for Solving 3-D, Time-Domain Maxwell Equations," AIAA Paper 92-0452, Jan. 1992.

[8]Shang, J. S., "A Fractional-Step Method for Solving 3-D, Time-Domain Maxwell Equations," AIAA Paper 93-0461, Jan. 1993.

[9]Steger, J. L., and Warming, R. F., "Flux Vector Splitting of the Inviscid Gasdynamic Equations with Application to Finite Difference Methods," *Journal of Computational Physics*, Vol. 40, No. 2, 1981, pp. 263–293.

[10]Roe, P. L., "Characteristic-Based Schemes for the Euler Equations," *Annual Review of Fluid Mechanics*, Vol. 18, 1986, pp. 337–365.

[11]MacCormack, R., "Current Status of Numerical Solutions of the Navier–Stokes Equations," AIAA Paper 85-0032, Jan. 1985.

[12]Anderson, W. K., Thomas, J. L., and van Leer, B., "A Comparison of Finite Volume Flux Vector Splittings for the Euler Equations," AIAA Paper 85-0122, Jan. 1985.

[13]Thomas, J. L., van Leer, B., and Walters, R. W., "Implicit Flux-Split Schemes for the Euler Equations," *AIAA Journal*, Vol. 28, No. 6, 1990, pp. 973, 974.

[14]Kroll, N., Gaitonde, D., and Aftosmis, M., "A Systematic Comparative Study of Several High Resolution Schemes for Complex Problems In High Speed Flows," AIAA Paper 91-0636, Jan. 1991.

[15]van Leer, B., "Flux-Vector Splitting for the Euler Equations," Institute for Computer Applications in Science and Engineering, Technical Rept. 82-30, Langley, Sept. 1982.

[16]Warming, R. F., and Beam, R. M., "On the Construction and Application of Implicit Factored Schemes for Conservation Laws," *Society for Industrial and Applied Mathematics Proceedings*, Vol. 11, 1978, pp. 85–129.

[17]Thomas, J. L., and Walters, R. W., "Upwind Relaxation Algorithms for the Navier Stokes Equations," AIAA Paper 85-1501, July 1985; also *AIAA Journal*, Vol. 25, No. 4, 1987, pp. 527–534.

[18]Fromm, J. E., "A Method for Reducing Dispersion in Convective Difference Schemes," *Journal of Computational Physics*, Vol. 3, 1968, pp. 176–189.

[19]Bagrinovskii, K. A., and Godunov, S. K., "Difference Schemes for Multi-Dimensional Problems," *Doklady Akademii Nauk USSR*, Vol. 115, 1957, p. 431.

[20]Carnahan, B., Luther, H. A., and Wilkes, J. O., *Applied Numerical Methods*, Wiley, New York, 1969.

[21]Jameson, A., "Multigrid Algorithms for Compressible Flow Calculations," *Lecture Notes in Mathematics*, Vol. 1228, 1986, pp. 166–201.